JOURNAL OF GEOPHYSICAL RESEARCH, VOL. 113, E08012, doi:10.1029/2007JE003037, 2008

Distribution of the ultraviolet nitric oxide Martian night airglow: Observations from Mars Express and comparisons with a one-dimensional model

C. Cox,[1] A. Saglam,[1] J.-C. Gérard,[1] J.-L. Bertaux,[2] F. González-Galindo,[3] F. Leblanc,[2,4] and A. Reberac[2]

Received 6 November 2007; revised 25 January 2008; accepted 2 April 2008; published 14 August 2008.

[1] Limb observations with the SPICAM ultraviolet spectrometer on board the Mars Express orbiter revealed ultraviolet nightglow emission in the δ (190–240 nm) and γ (225–270 nm) bands of nitric oxide. This emission arises from radiative recombination between O(^{3}P) and N(^{4}S) atoms that are produced on the day side and form excited NO molecules on the night side. In this study, we analyze the night limb observations obtained during the MEX mission. In particular, we describe the variability of the emission brightness and its peak altitude. We examine possible correlations with latitude, local time, magnetic field strength or solar activity. We show that the altitude of maximum emission varies between 55 and 92 km while the brightness is in the range 0.2 to 10.5 kR. The total vertical emission rate ranges from 8 to 237 R with an average value of 36 ± 52 R. The observed topside scale height of the emission profile varies between 3.8 and 11.0 km, with a mean value of 6 ± 1.7 km. We use a chemical-diffusive atmospheric model where the eddy coefficient, whose value in the Mars thermosphere is uncertain, is a free parameter to match the observed peak altitude of the emission. The model solves the continuity equation for O(^{3}P), N(^{4}S), and NO using a finite volume method on a one-dimensional grid. We find that the downward flux of N atoms at 100 km varies by two orders of magnitude, ranging from 10^7 to 10^9 atoms cm^{-2} s^{-1}.

Citation: Cox, C., A. Saglam, J.-C. Gérard, J.-L. Bertaux, F. González-Galindo, F. Leblanc, and A. Reberac (2008), Distribution of the ultraviolet nitric oxide Martian night airglow: Observations from Mars Express and comparisons with a one-dimensional model, *J. Geophys. Res.*, *113*, E08012, doi:10.1029/2007JE003037.

1. Introduction

[2] The nitric oxide ultraviolet airglow has been observed on the night side of all three terrestrial planets. Its presence was first detected on Earth by *Cohen-Sabban and Vuillemin* [1973] during balloon flights. On Venus, the same emission was both observed and identified by *Stewart et al.* [1979] during the Pioneer Venus mission and by *Feldman et al.* [1979] using IUE. More recently, it has been detected on Mars by *Bertaux et al.* [2005] using the SPICAM (Spectroscopy for Investigation of Characteristics of the Atmosphere of Mars) spectrograph on board the Mars Express (MEX) spacecraft. The emission process is radiative recombination of nitrogen N(^{4}S) and oxygen O(^{3}P) atoms giving excited NO ($C^2\Pi$) molecules which emit directly in the ultraviolet δ bands and in the γ bands through the $A^2\Sigma$, $v' = 0$ state:

$$
\begin{aligned}
N(^4S) + O(^3P) &\rightarrow NO(C^2\Pi)\\
NO(C^2\Pi) &\rightarrow NO(X^2\Pi) + \delta bands\\
NO(C^2\Pi) &\rightarrow NO(A^2\Sigma, v' = 0) + 1.22\mu\mathrm{m}\\
NO(A^2\Sigma, v' = 0) &\rightarrow NO(X^2\Pi) + \gamma bands
\end{aligned}
$$

[3] Note that the 1.22 μm emission is exactly as intense as the gamma bands since this state is only populated by cascades from the $C^2\Pi$ state. As a consequence of these processes, the total ultraviolet emission rate is proportional to the rate of recombination of O and N atoms and thus depends on the nitrogen and oxygen densities. The nightglow intensity therefore reflects these densities on the nightside of the planet considered. Horizontal advection and subsolar to antisolar circulation transport are the main mechanisms that carry N and O atoms from the dayside. O atoms are produced by photodissociation of CO_2, CO and O_2 to a lesser extent whereas N atoms originate from photo- and electron impact dissociation of N_2 and ion reactions. The corresponding densities and fluxes are regulated by dynamics on the nightside which brings winds and eddy diffusion into play. Observations and calculations of densi-

[1] LPAP, Université de Liège, Liège, Belgium.
[2] Service d'Aéronomie, Université Versailles Saint Quentin, CNRS, Verrières-le-Buisson, France.
[3] Laboratoire de Météorologie Dynamique, CNRS, Paris, France.
[4] Now at Osservatorio Astronomico di Trieste, INAF, Trieste, Italy.

0148-0227/08/2007JE003037$09.00

ties can therefore help to estimate these essential dynamical quantities.

[4] Evaluation of the eddy diffusion coefficient and calculation of the densities and fluxes on Mars are the two main objectives of this study. Estimates of the eddy diffusion coefficient have been made by *Kahn* [1990], who claims that it may vary by up to three orders of magnitude. *Nair et al.* [1994] have proposed an eddy diffusion profile based on one-dimensional photochemical models that have been developed over the last 30 years. The K values range from 10^5 to 10^8 cm^2 s^{-1} in the dayside lower atmosphere (below 100 km) [*McElroy and Donahue*, 1972; *Liu and Donahue*, 1976; *Kong and McElroy*, 1977; *Yung et al.*, 1988; *Krasnopolsky and Parshev*, 1979; *Shimazaki*, 1989; *Krasnopolsky*, 1993; *Atreya and Gu*, 1994]. *Krasnopolsky* [2002] used a coefficient proportional to the inverse of the square root of the total density for altitudes higher than 80 km. He modeled the Martian photochemistry [*Krasnopolsky*, 2006] and also proposed a new profile ranging from 3×10^6 cm^2 s^{-1} to 10^7 cm^2 s^{-1} for the lower atmosphere.

2. Observations

[5] SPICAM is an ultraviolet and infrared spectrometer on board the Mars Express spacecraft. Its ultraviolet domain ranges from 118 nm to 320 nm and includes the NO δ ($C^2\Pi \rightarrow X^2\Pi$) and γ ($A^2\Sigma \rightarrow X^2\Pi$) emission bands. SPICAM observations cover different Martian seasons and a wide range of local times and latitudes. The altitudes scanned by the line of sight are typically between 10 km and 400 km on Mars' limb. The MEX spacecraft followed an almost polar eccentric orbit with a 6.72 h period with the pericenter and apocenter positioned at 298 km and 10,107 km respectively. The precession of the orbital plane lead to a wide variety of observation configurations on the night side as well as on the day side. A total of 21 orbits contain useful nightglow observations. These observations were performed in the grazing (tangential) limb mode where the time of observation of the limb is greater than that in the usual limb observations in the orbital plane. Limb observations are generally used to collect a strong signal despite their particular pointing geometry. The signal recorded by the CCD detector is typically integrated over 1 s periods for about 20 min for each orbit.

[6] The observations were carried out according to the following method: after each integration, a section of the CCD detector is spatially divided into five adjacent parts each one containing a number of spectra equal to the preselected BIN parameter (2, 4, 8, 16 or 32). These lines are either seen through a small (50 μm) or a large (500 μm) slit, determining the spectral resolution of the instrument. These spectra are averaged and thus provide 5 sets (the five spatial bins) each second corresponding to 5 different, but adjacent, altitude, latitude, local time and solar zenith angle ranges taken at the tangent point. The distance from the spacecraft to the tangent point, the pixel field of view of 0.7 arcmin and the spatial binning of 2, 4, 8, 16 or 32 lines lead to a limb spatial resolution typically equal to a few kilometers or less. During the orbit, each averaged spectrum corresponding to the same spatial bin is stored in an array called ''tempo-image''. Therefore the tempo-images are defined as five arrays, each one containing about a thousand spectra associated with the same number of different altitudes. Altogether, no less than 5000 spectra are recorded by SPICAM during a single orbit.

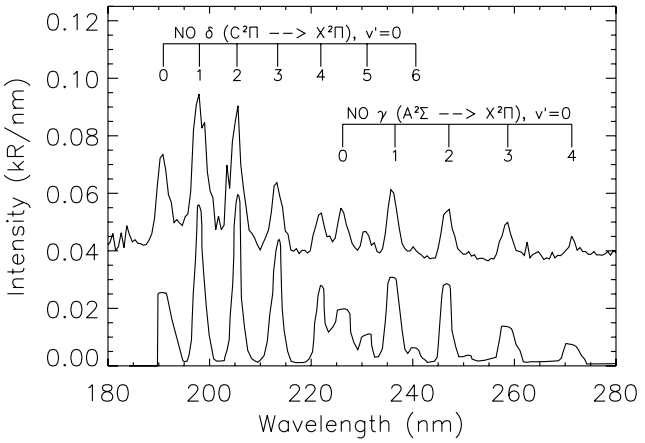

Figure 1. Top: SPICAM spectrum summed over 1060 lines of orbit 734 first and second tempo-images. Bottom: Laboratory spectrum [*Groth et al.*, 1971] plotted at the SPICAM spectral resolution.

[7] Following the method described by *Leblanc et al.* [2006] the spectrum of each tempo-image is cleansed of nonuniform dark current (DCNU), offset, light scattering, and is background-subtracted. DCNU and offset are removed using technical observations executed with a low amplifier voltage. The absolute calibration is obtained using well-known hot star spectra; the pixel intensities are converted as follows:

$$I_{kR/nm} = \frac{10^{-9} 4\pi I_{ADU}}{G\ \sigma\ d\lambda\ \Omega\ dt} \tag{1}$$

with

$$\Omega = \frac{l_{px} l_{slit} BIN}{f^2} \tag{2}$$

where $I_{kR/nm}$ is the pixel intensity in kR nm^{-1}, I_{ADU} is the pixel intensity in ADU (Analog to Digital Unit), G is the gain of the amplified CCD in ADU by photoevent, σ is the surface efficiency of the instrument, Ω is the solid view angle of a pixel, $d\lambda$ is the pixel size in wavelength units, dt is the integration time (less than 1 s), l_{px} is the pixel size in μm, l_{slit} is the slit size (50 μm or 500 μm) and f is the focal length.

[8] For this study, we have integrated each spectrum over the entire δ and γ bands emission between 190 nm and 260 nm. Figure 1 shows a comparison between a sum of more than one thousand SPICAM spectra and a laboratory spectrum. The comparison indicates that the Mars nightglow ultraviolet spectrum shows the δ and γ bands arising from the $v' = 0$ vibrational level of the $C^2\Pi$ and $A^2\Sigma^+$ states of NO. We have not identified any other emissions in the observed spectrum. Integration over this spectral domain provides the brightness in kR for each scanned altitude. The line of sight crosses the same altitudes twice, once during the ingress segment and once during the egress segment. Then, owing to the geometry of the grazing limb observation

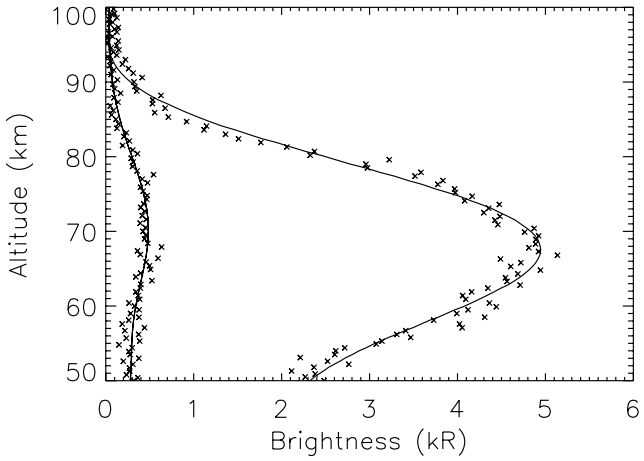

Figure 2. Airglow limb profiles obtained on orbit 734. The weaker profile corresponds to the ingress segment of the line of sight, whereas the stronger comes from the egress part. Xs represent raw observed intensities and the solid lines are the smoothed profiles.

type, SPICAM supplies two sets of five (for the five spatial bins) altitude profiles at each orbit. To remove the statistical noise and to obtain clearly peaked curves, the altitude profiles are smoothed using a low-pass filter. Figure 2 shows the limb profile of the NO nightglow measured on the ingress and egress segments of orbit 734 (X symbols). The solid lines are smoothed fits obtained by applying the lowpass filter to the individual data points. This filter is adjusted in order to get a curve showing one single peak. The latitudes of the ingress and egress are 30.9°S and 58°S respectively and the local times are 20.3 and 21.8 LT. The peak intensities are 0.5 and 4.9 kR, which illustrates the non uniformity of the NO airglow distribution.

[9] Each observed limb profile can be characterized by the altitude, brightness and observing conditions such as solar longitude, latitude and local time of the maximum emission brightness. In order to provide additional information, we sought to fit the data points of each limb profile with an integrated Chapman curve:

$$I(z_{tg}) = 2\int_{z_{tg}}^{\infty} \frac{z}{\sqrt{z^2 - z_{tg}^2}} P(z)dz \qquad (3)$$

with

$$P(z) = P_m \exp\left(1 - \frac{z - z_m}{H} - \exp\left(-\frac{z - z_m}{H}\right)\right) \qquad (4)$$

and

$$H = H_m + a(z - z_m) \qquad (5)$$

where the fit parameters are z_m the peak altitude, P_m the peak emission rate, H_m the scale height above the peak and a, a coefficient of linear dependence between the scale height and the altitude. $I(z_{tg})$ is the brightness at z_{tg}, the tangent point along the line of sight and $P(z)$ is the emission rate at the altitude z. The factor of 2 arises from the symmetry of the geometry. More precisely, it corresponds to emission originating from behind as well as above the tangent point. Function (3) is then convolved by the instrument field of view before fitting. From these fits we determine the scale height of the emission as well as the total vertical brightness. All the values for these quantities are given in Table 1. Values deduced from profiles with errors larger than 10% are not given. The mean error on the fit is about 5%. We deliberately chose not to represent all the data available for the NO emission. The numbers provided for each egress/ingress segment of orbit correspond to one of the five profiles available. We do so either because the other profiles related to the other tempo-images are very similar to the selected one or because their signal-to-noise ratios are too small (i.e., when the small slit is used). We found about ten orbits when SPICAM was observing the Mars nightside and where no measurable NO emission was present. The latitudes and local times scanned by the line of sight during these observations are spread over the night hemisphere which explains in part the high variability of the emission brightness.

[10] If orbits with no measurable signal are taken into account, setting their brightness equal to the instrument detectability threshold (0.1 kR for limb scans) or equal to zero (see Table 1), the average altitude and brightness of the peak are respectively 73.0 ± 8.2 km and 1.2 ± 1.5 kR. The average vertical brightness is obtained in the same way and is equal to 36 ± 52 R.

3. Correlations

[11] We first notice in Table 1 the large variations between the values measured on the different limb profiles. The brightness of the profile peaks observed by the instrument varies up to two orders of magnitude and the corresponding altitudes change in a 35 km range. Therefore we have searched for any correlations that may exist between the values of the last six columns and the geometrical parameters of the observations. Geometric parameters that could possibly control the emission profiles are latitude, local time and the different seasons represented by four intervals of solar longitude (LS). The ranges of latitudes and local times covered by the observation set are shown in Figure 3 which represents the distribution of data. We note that there is no data point later than 2:00 LT nor at latitudes higher than 60°N or S. The circles, which characterize zones with emission profiles presenting no peak, are spread all over the map. As we discussed below, this may be consistent with the highly unpredictable and variable behavior of the Martian nightglow. The latitudes vary from 59.3°S to 60.9°N. In this interval, we have analyzed the variability of the brightness and of the peak altitude. First, we have found no clear trend in the brightness variation, as shown in Figure 4. The only conclusion that can be drawn is that the higher values are located near 60°S while the weaker ones are spread over the whole range of latitudes. We note that points of highest brightness belong to the spring season in the southern hemisphere (Ls = [180, 270]°). If we now consider the plot of peak altitudes as a function of latitude shown in Figure 5, we observe two trends in the northern and in the southern hemisphere respectively. The first one is made of data points corresponding to solar longitude Ls

Table 1. SPICAM NO Airglow Observations: Characteristics of the Limb Profiles

Orbit	Date	LS, deg	F10.7	Spatial BIN	Orbit Segment	Latitude, deg	Local Time, h	Peak Brightness, kR	Peak Altitude, km	Peak emiss. Rate,[a] R/km	Emission Rate Peak Altitude,[a] km	Scale Height,[a] km	Vertical Brightness[a] (R)
0716A01	11 Aug 2004	72.5	107.2	5	ingress	−33.7	20.5	1	70.6	1.88	74.9	4.95	28.1
	11 Aug2004	72.5	107.2	5	egress	−59.1	22.1	8.13	61.6	14.39	65.9	5.90	236.8
0734A01	16 Aug2004	74.7	87.7	5	ingress	−30.9	20.3	0.48	70	0.79	75.5	6.97	15.4
	16 Aug 2004	74.7	87.7	5	egress	−58	21.8	4.94	67.3	7.85	73	7.48	162.5
1563A01	5 Apr 2005	187.7	78.6		ingress								
	5 Apr 2005	187.7	78.6	5	egress	60.9	1.7	2.45	66.8	5.13	69.4	4.43	59
1577A01	9 Apr 2005	190	80.2	5	ingress	28.3	0.5	0.39	73.3	0.68	76.5	6.23	11.5
	9 Apr 2005	190	80.2	5	egress	57.9	1.3	1.34	55.3	2.27	59.6	6.42	39.6
1599A01	15 Apr 2005	193.6	87.9	5	ingress	13.6	0.3	3.69	80.7	6.65	85.5	5.51	107.8
	15 Apr 2005	193.6	87.9	3	egress	49.2	0.3	0.58	73.4	0.88	77.7	8.07	19.4
1782A01	5 Jun 2005	224.6	99	5	ingress	20.1	20.8	0.45	91	1.09	92.2	3.70	17.7
	5 Jun 2005	224.6	99	5	egress	51.3	21.9	0.56	67.8	0.82	71.6	7.46	28.5
2535A01	2 Jan 2006	350.2	81.2	4	ingress	−7.46	1.1	1.07	69.6	1.58	72.2	7.36	49.3
	2 Jan 2006	350.2	81.2		egress								
2611A01	23Jan 2006	1.005	84.2		ingress								
	23 Jan 2006	1.005	84.2	4	egress	−0.71	0.2	2.03	65.6	2.34	67.2	11.04	155.1
2615A01	24 Jan 2006	1.560	81		ingress								
	24 Jan 2006	1.560	81	4	egress	−2.12	0	1.92	85.6	3.58	91	3.98	58.4
2620A01	26 Jan 2006	2.253	77.2		ingress								
	26 Jan 2006	2.253	77.2	4	egress	5.18	0.3	0.57	63.9	···	···	···	···
2623A01	27 Jan 2006	2.669	76.5		ingress								
	27 Jan 2006	2.669	76.5	4	egress	4.48	0.2	0.51	76.5	···	···	···	···
2625A01	27 Jan 2006	2.946	76.5		ingress								
	27 Jan 2006	2.946	76.5	4	egress	4.49	0.2	0.18	79	···	···	···	···
2645A01	2 Feb 2006	5.704	74.2		ingress								
	2 Feb 2006	5.704	74.2	4	egress	3.05	23.8	1.46	73.1	···	···	···	···
2771A01	9 Mar 2006	22.60	72.8	4	ingress	−30	20.9	0.28	83.2	0.49	89.6	3.77	9.56
	9 Mar 2006	22.60	72.8	4	egress	−53.9	22	1.23	64.9	2.48	68.1	4.53	30.7
2800A02	17 Mar 2006	26.38	75.4	5	ingress	−28.8	20.6	2.40	70.1	···	···	···	···
	17 Mar 2006	26.38	75.4		egress								
2832A01	26 Mar 2006	30.51	86.1	5	ingress	−24.4	20.2	1.46	64.1	3.13	67.3	3.86	35.2
	26 Mar 2006	30.51	86.1		egress								
2900A02	14 Apr 2006	39.15	79.3	5	ingress	−34.3	19.7	1.40	83.7	2.67	88.1	4.79	38.7
	14 Apr 2006	39.15	79.3	5	egress	−46.3	21.4	1.08	76.1	1.87	81.3	6.25	33.3
2966A02	3 May 2006	47.43	79.8	2	ingress	−31.7	23.5	0.92	72	···	···	···	···
	3 May 2006	47.43	79.8		egress								
2987A01	9 May 2006	50.04	73.1	1	ingress	−33.1	23.1	3.28	61.3	···	···	···	···
	9 May 2006	50.04	73.1	1	egress	−8.81	0.2	2.30	87.2	···	···	···	···
2988A01	9 May 2006	50.15	73.1	4	ingress	−36.69	20.1	1.36	72.7	2.26	76.8	6.64	40.7
	9 May 2006	50.15	73.1	4	egress	−39.32	21.2	2.30	72.2	4.03	75.8	6.01	65.3
3007A02	14 May 2006	52.50	79.4	5	ingress	−26.03	18.8	0.30	77.4	0.57	81.1	5.10	8
	14 May 2006	52.50	79.4	5	egress	−36.53	20.1	1.55	80.8	2.53	85.3	6.94	47.5
Mean values calculated for this array of data (using 0.1 kR for observations presenting no measurable NO):								1.18 kR ± 1.53	73 ± 8.2	1.97 ± 2.81	76.8 ± 8.8	5.97 ± 1.7	36.2 ± 51.8
Mean values calculated for this array of data (using 0 kR for observations presenting no measurable NO):								1.15 kR ± 1.55	73 ± 8.2	1.89 ± 2.86	76.8 ± 8.8	5.97 ± 1.7	35.1 ± 52.5

Note: Cells with no value (···) correspond to data which cannot be fitted with the Chapman function. Grey cells show orbit part where observation was not performed or where no measurable NO was present.

[a]From Chapman function.

ranging from 185°to 225° (fall) whereas the second one corresponds to the 35°–75° (spring). The points are too widespread to provide a reasonable regression curve but the higher the latitude, the lower the altitude of the peak. However, we have noted that the few data points belonging to the other seasons (i.e., solar longitude) and which are centered near the equator do not show the same trend. This decrease of the altitude of the peak when moving to higher latitudes could be linked to the behavior of constant pressure surfaces. However, studies with the LMD-MGCM model show that, although there is a decrease of the altitude of the isobars with increasing latitudes for both of the seasons, this decrease is mostly confined to latitudes higher than 50° and its magnitude is about 10 km. So, this effect is only a contribution to the variation of the peak altitude with latitude. Other processes, possibly of a dynamic nature, must be acting here. We thus conclude that latitude can play a role in the distribution of the nightglow layer, depending on the season. Such a correlation can only be revealed by a global three-dimensional photochemical model.

[12] We examine a possible correlation between the peak emission intensity and its altitude. The result is represented in Figure 6. As mentioned at the beginning of this section, we notice that the peak brightness intensity varies from 0.2 to 10.5 kR whereas the peak altitude varies between 55 and 92 km. The highest intensities are generally associated with low altitudes but there is no real systematic dependence between the peak altitude and the peak brightness. Actually, highest intensity points could be the result of their latitude (near 60°S) or local time position (near 22:00 LT) and no

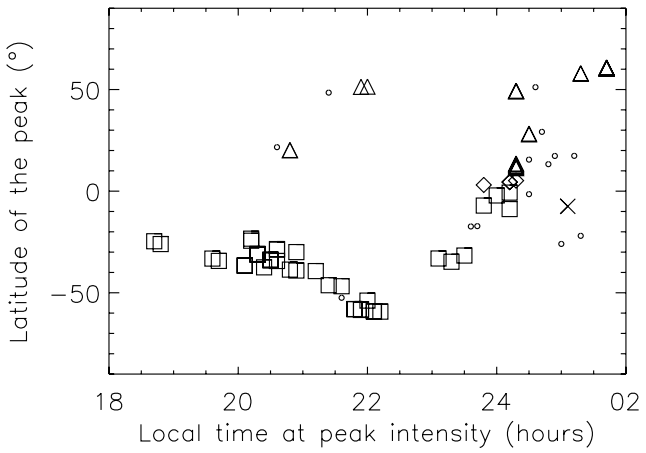

Figure 3. Map of the locations of the individual observations. Diamonds represent spring season data in the northern hemisphere (Ls = [0, 90]°), triangles are fall data in the northern hemisphere (Ls = [180, 270]°), squares are spring season observations in the southern hemisphere (Ls = [180, 270]°), crosses correspond to winter season data in the southern hemisphere (Ls = [90, 180]°). Small circles correspond to data presenting no peak, typically below 0.5 kR, whatever the season.

element in this study makes it possible to discriminate between the controlling factors. A more detailed analysis of the control by individual factors would require considerably more data points spread homogeneously over the different ranges of the possible parameters. We also compared the distribution of emission peak altitude and brightness with the intensity of the Martian magnetic field normalized at 200 km [*Purucker et al.*, 2000] which has been mapped with Mars Global Surveyor. This study

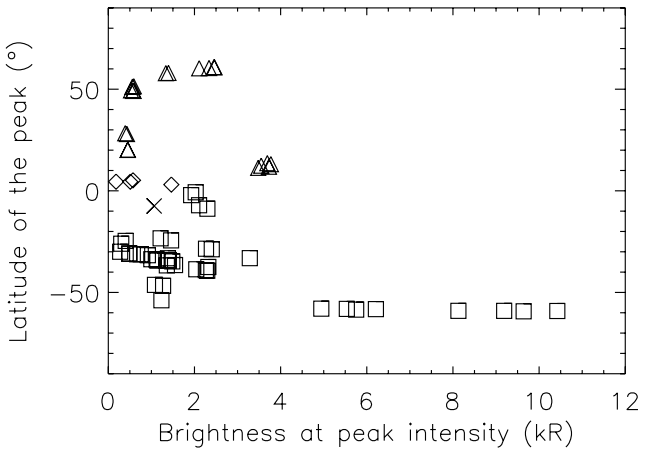

Figure 4. Variation of peak brightness as a function of latitude. High brightness intensities are located near 60°S. Diamonds are spring season data in the northern hemisphere (Ls = [0, 90]°), triangles are fall season data in the northern hemisphere (Ls = [180, 270]°), squares are spring season data in the southern hemisphere (i.e., fall in the northern one (Ls = [180, 270]°)) and crosses are winter season data in the southern hemisphere (i.e., summer in the northern one (Ls = [90, 180]°)).

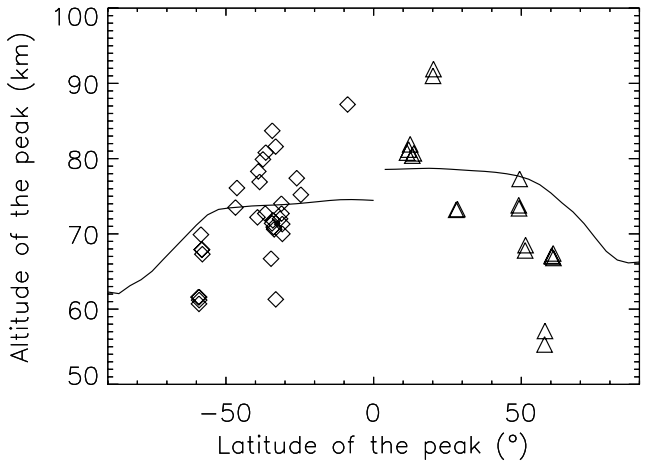

Figure 5. Variation of peak altitudes as a function of latitude. Diamonds are data of LS = [35, 75]° and triangles are data of LS = [185, 225]°. The black lines represent the 0.1 Pa isobars for LS = 40° (left) and LS = 190° (right).

showed that no correlation could be found between these quantities.

[13] Because of the solar dependent nature of the nitrogen and oxygen production on the dayside, it is relevant to study a possible correlation between the airglow intensity and the solar activity. To do so, we use the F10.7 index values (in 10^{-22} W/m^2/Hz) calculated from daily average, taking into account the relative positions of the Earth and Mars and the solar rotation (see Table 1). We have plotted the brightness of the limb observations versus the corresponding F10.7. Even though the strongest brightness intensity is linked to the highest F10.7 index, we have found no clear dependence (correlation coefficient r = 0.31). This can be partly explained by the fact that NO emission is not homogeneously spread on the nightside hemisphere but shows

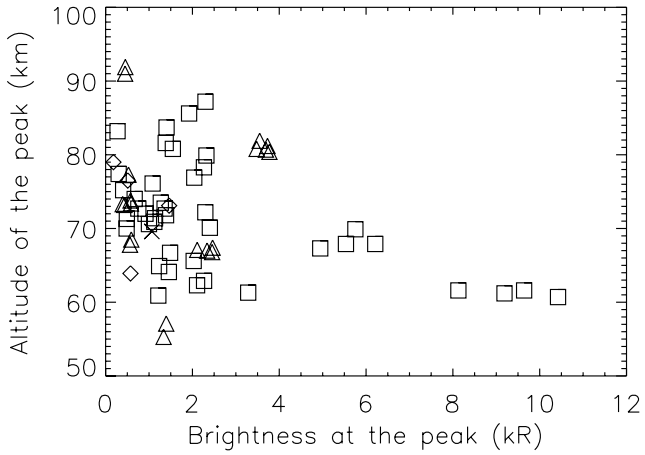

Figure 6. Variation of peak altitude as a function of peak brightness. All the sets of available data are represented on this graphic. High brightness intensities are linked to low altitudes (under 70 km). Diamonds are spring season data in the northern hemisphere, triangles are fall season data in the northern hemisphere, squares are spring season data in the southern hemisphere and crosses are winter season data in the southern hemisphere.

Table 2. Table of Chemical Reactions and Rate Coefficients

#	Reaction	Rate	Reference
1	$N + O \rightarrow NO + h\nu$	$1.92 \times 10^{-17} \times (300/T)^{1/2} \times (1\text{-}0.57/T^{1/2})$ cm^3 s^{-1}	*Dalgarno et al.* [1992]
2	$N + O + CO_2 \rightarrow NO + CO_2$	2×10^{-32} $(300/T)^{1/2}$ cm^6 s^{-1}	*Campbell and Thrush* [1966]
3	$N + NO \rightarrow N_2 + O$	$2.5 \times 10^{-10} \times (T/300)^{1/2} \times \exp(-600/T)$ cm^3 s^{-1}	*Fox* [1994]
4	$O + O + CO_2 \rightarrow O_2 + CO_2$	2.8×10^{-32} cm^6 s^{-1}	*Campbell and Gray* [1973][a]
5	$O_2 (^1\Delta) + CO_2 \rightarrow O_2 + CO_2^*$	3×10^{-20} cm^3 s^{-1}	*Yung and Demore* [1982]
6	$O_2 (^1\Delta) \rightarrow O_2 + h\nu$	2.19×10^{-4} s^{-1}	*Newman et al.* [1999]

[a]This value has been multiplied by 2.5 to take into account the CO_2 efficiency in the three body reaction [*Nair et al.*, 1994].

patchy emission with some areas stronger than others. SPICAM only scans a small fraction of the nightside which does not represent the hemisphere average. Moreover the observations have been performed during different Mars seasons (i.e., LS values) and their number is too small to provide a definite conclusion on a possible correlation.

4. Modeling

[14] The development of a one-dimensional model is motivated by the presumed presence of a downward flux of nitrogen and oxygen atoms which recombine to produce the NO airglow emission. By analogy to the case of Venus, *Bertaux et al.* [2005] suggested that a global transport mechanism similar to the subsolar to antisolar circulation could occur on Mars, despite the fact that the atmosphere is clearly subjected to a much faster diurnal solar illumination cycle than Venus. This model brings into play advection/diffusion equations as well as loss and creation chemical reactions. The continuity equation for a minor constituent i may be written:

$$\frac{\partial n_i}{\partial t} = -\frac{\partial \phi_i}{\partial z} + P_i - L_i - \frac{\partial (n_i w)}{\partial z} \tag{6}$$

with the vertical diffusive flux Φ_i of a minor constituent i given by:

$$\phi_i = -(D_i + K)\left(\frac{\partial n_i}{\partial z} + \frac{n_i}{T}\frac{\partial T}{\partial z}\right) - \left(\frac{D_i}{H_i} + \frac{K}{H}\right) n_i \tag{7}$$

where D_i is the molecular diffusion coefficient for constituent i, K is the vertical eddy diffusion coefficient, H_i is the local scale height of the ith constituent, H is the atmospheric scale height, T is the neutral gas temperature, n_i is the number density of the ith species, z is the altitude, t is the time, P_i is the production rate of species i, L_i the loss rate and w is the vertical velocity positive upward. The last term in equation (6) corresponds to the vertical advective flux. We use a vertical variation of the eddy diffusion coefficient (K) similar to the one used on Venus [*Von Zahn et al.*, 1979; *Gérard et al.*, 1981], that is:

$$K(z) = \frac{A}{\sqrt{n(z)}} \text{cm}^2 \text{ sec}^{-1} \tag{8}$$

where n is the total number density and A is a free parameter of the model which is constant with respect to altitude. Therefore K only depends on the altitude and is identical for all constituents. The molecular diffusion coefficient D_i is given by *Banks and Kockarts* [1973]:

$$D_i(z) = 1.52\, x\, 10^{18} \frac{\sqrt{T(z)\left(\frac{m_0}{m} + \frac{m_0}{m_1}\right)}}{n(z)} \text{ cm}^2 \text{ sec}^{-1} \tag{9}$$

where m_0, m_i and m are respectively the mass of a hydrogen atom, the species molecular weight and the mean molecular mass of the Martian atmosphere, taken here equal to 43 g mol^{-1} and constant with altitude. The model solves equation (6) for O(^{3}P), N(^{4}S), NO and O_2 ($^1\Delta$). This last species has been introduced in the general model for future studies of the 1.27μm emission on the Venus nightside. The P_i and L_i coefficients depend on the choice of the different reactions that come into play and which are described in Table 2 with their corresponding reaction rates. Equation (6) is solved numerically between 30 and 100 km using the finite volume method on a constant grid. Therefore equation (6) for an arbitrary constituent integrated on a cell volume of Δz vertical length becomes:

$$\frac{\partial n_m}{\partial t}\Delta z = -[\phi]_{m-\frac{1}{2}}^{m+\frac{1}{2}} + (P_m - L_m)\Delta z - [nw]_{m-\frac{1}{2}}^{m+\frac{1}{2}} \tag{10}$$

and using a forward discretization for the time derivative, we get:

$$n_m^{l+1} = \frac{\Delta t}{\Delta z}\left(\frac{\Delta z}{\Delta t} n_m^l - \left[\phi^l\right]_{m-\frac{1}{2}}^{m+\frac{1}{2}} + \left(P_m^l - L_m^l\right)\Delta z - \left[n^l w\right]_{m-\frac{1}{2}}^{m+\frac{1}{2}}\right) \tag{11}$$

where m and l are respectively the spatial and the time indexes and Δt is the time elapsed between time l and $l + 1$. We then iterate equation (11) until the following criterion is reached for each specie,

$$\frac{n_m^{l+1} - n_m^l}{n_m^{l+1}} \leq 10^{-4} \tag{12}$$

and keeping the boundary conditions constant for each time step. For the different constituents, we apply the

Table 3. Boundary Conditions

Constituent	z = 30 km	z = 100 km
N(^{4}S)	$n = n_{N(4S),0}$	$\phi = \phi_{N(4S),N}$
O(^{3}P)	$n = n_{N(3P),0}$	$\phi = 100x\ \phi_{N(4S),N}$
NO	$n = n_{NO,0}$	$\phi = 0$
O_2 ($^1\Delta$)	$n = n_{O2(1\Delta),0}$	$\phi = 0$

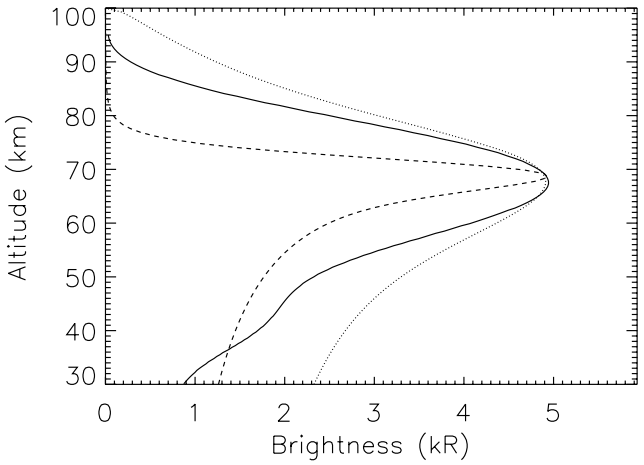

Figure 7. Orbit 734 limb profile. The dark line represents the observation, the dotted line is the model with w(z) = 0 and the dashed line is the model profile with w(z) taken from the LMD 3-D model.

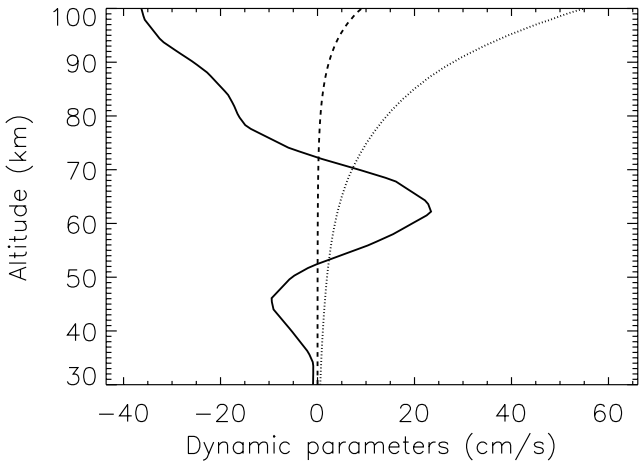

Figure 9. The figure shows the three different dynamic parameters for orbit 734. The black line is the LMD w(z) profile, the dotted line is the eddy diffusive velocity K(z)/H(z) profile used and the dashed line is the variation of the molecular diffusion velocity D(z)/H(z) for oxygen.

conditions listed in Table 3, and we use density null vectors for initial conditions (except for boundary limits). Our model is then parameterized by A, w(z) and Φ_N. In fact, the choice of the $n_{(z=30km)}$ parameter does not influence the solution if it is kept in a reasonable range. At the upper boundary, we adopt a $O(^3P)$ flux equal to a hundred times the $N(^4S)$ flux. This ratio is deduced from several attempts to obtain realistic density curves in our model and oxygen profiles similar to those of *Krasnopolsky* [2006]. The stability of the convergence is guaranteed by the Courant-Friedrichs-Lewy (CFL) criterion which can be written:

$$\Delta t \leq \frac{\Delta z}{(K+D)_{\max}} \tag{13}$$

which therefore determines the time step. We use a vertical step Δz of 0.5 km and a time step Δt equal to 99% of the right hand side of the inequality (13).

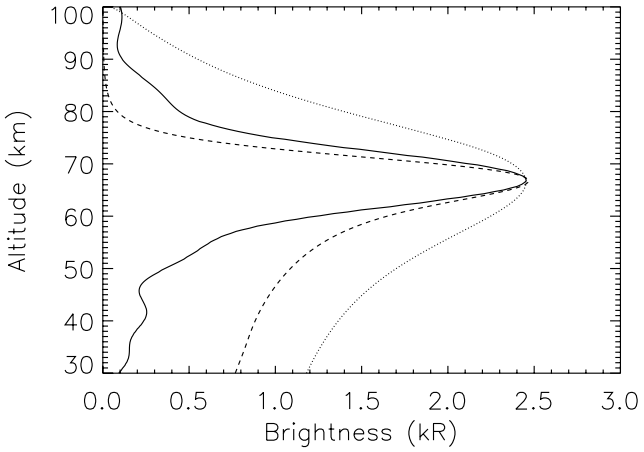

Figure 8. Orbit 1563 limb profile. The dark line represents the observation, the dotted line is the modeled distribution with w(z) = 0 and the dashed line is calculated with w(z) taken from the LMD 3-D model.

[15] As reaction (1) of Table 2 is the only one which produces NO photons, the limb profile of the nitric oxide emission is obtained by integrating the product of [O], [N] and k along the line of sight, where k is the first rate constant of Table 2. This provides numerical values of the column emission rate (in cm^{-2} s^{-1}) to be multiplied by 10^{-6} to express them in Rayleigh units.

[16] Before comparing observed and calculated limb profiles, we first examine the position of the homopause limit that can be deduced from our CO_2 and T profiles by equating equations (8) and (9). This always leads to an altitude higher than 100 km, indicating that the modeled region is entirely located in the homosphere. One-dimensional models usually do not include advection terms. Consequently, in this representation, vertical transport is solely the result of the molecular and eddy diffusions, and advection is implicitly contained in the K coefficient, despite the lack of physical meaning. However, we also present two case studies with $w(z) \neq 0$ in order to examine the effects of explicitly including a vertical wind velocity. We first show the result of some modeled limb profiles using a CO_2 and temperature background provided by the ground-to-thermosphere General Circulation Model for Mars developed at the Laboratoire de météorologie dynamique (LMD, Paris) [*Forget et al.*, 1999; *Angelats i Coll et al.*, 2005]. Figures 7 and 8 show modeled profiles for the fifth spatial bin band of orbits 734 and 1563. They match the peaks of the observed profiles reasonably well. For w(z) = 0, the oxygen fluxes used at the top boundary to model orbits 734 and 1563 are respectively 3.8×10^{10} and 2.0×10^{10} cm^{-2} s^{-1} and 1% of these values for the nitrogen fluxes. Likewise, the applied coefficients A in the eddy diffusion formula are respectively 6.4×10^{12} and 5.6×10^{12} providing values of 8.4×10^5 and 5.9×10^5 cm^{-2} s^{-1} for K at peak altitudes of 67.3 km and 66.8 km. According to the photochemical model of *Nair et al.* [1994], the column rates of CO_2 and O_2 photodissociation are equal to 1.1×10^{12} cm^{-2} s^{-1} and 2.1×10^{11} cm^{-2} s^{-1}

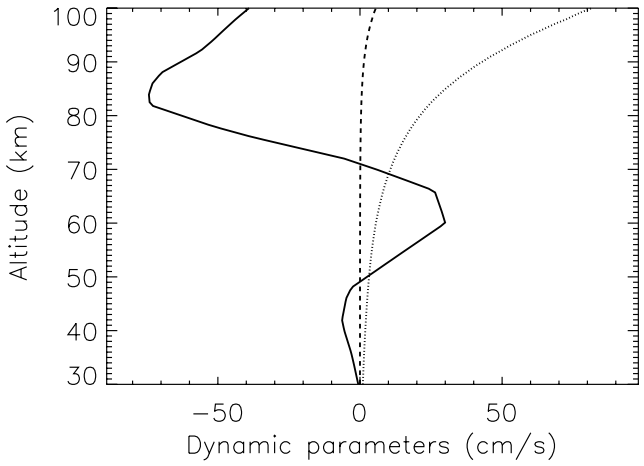

Figure 10. The figure shows the three different dynamic parameters for orbit 1563. The black line is the LMD w(z) profile, the dotted line is the eddy diffusive velocity K(z)/H(z) profile used and the dashed line is the variation of the molecular diffusion velocity D(z)/H(z) for oxygen.

respectively. These rates provide a total oxygen production of 1.3×10^{12} cm^{-2} s^{-1}. The production of oxygen atoms available for transport to the nightside has to be considered above 80 km where it becomes about a quarter of the previous calculated value [*Krasnopolsky*, 2006], that is 3.3×10^{11} cm^{-2} s^{-1}. This is large enough (about ten times) to balance the fluxes needed at the model upper boundary. Moreover, we point out that the calculated nitrogen production of 2.8×10^{9} cm^{-2} s^{-1} is mostly spent to form NO molecules on dayside which is the dominant odd nitrogen species in the upper atmosphere of Mars according to the Viking measurements [*Fox*, 1996]. The remaining nitrogen atoms are then mostly consumed in their reaction with NO on the dayside and the expected flux on the nightside is lower, that is $\sim 10^{7}$. This mean value is clearly too small to balance the flux of nitrogen required on the night side and deduced from orbit 734 and 1563. However, note that orbits 734 and 1563 are among the brightest in the data set. If we express that the flux of N atoms is consumed by reactions (1) and (2):

$$\phi_N = -2x \int_{z=30\text{km}}^{z=100\text{km}} (k_1 + k_2[CO_2])[O][N]dz \qquad (14)$$

neglecting the three-body recombination process which contributes less than 2 % at the peak altitude, we found that:

$$\phi_N \approx -2x \int_{z=30\text{km}}^{z=100\text{km}} k_1[O][N]dz = -2xI_{NO*}^{vertical} \qquad (15)$$

where $I_{NO*}^{vertical}$ is the vertical total emission rate. Using the mean value of the vertical nightglow intensity deduced from Table 1 in equation (15), we obtain a mean downward nitrogen flux of 7×10^{7} cm^{-2} s^{-1} which is closer to the nitrogen remaining flux coming from the dayside and which is equal to 2.5 % of the total dayside nitrogen production rate.

[17] In the case of w(z) $\neq$ 0 we obtain 2.0×10^{10} cm^{-2} s^{-1} for orbit 734 and 2.5×10^{10} cm^{-2} s^{-1} for orbit 1563 for the total oxygen flux, a hundred times less for the total nitrogen flux, 4.0×10^{13} and 7.0×10^{13} for the A parameter, and 5.3×10^{6} and 9.1×10^{6} for the K coefficient at the same peak altitudes. These last values of K are very large and stem from the fact that, at the peak altitudes considered, the modeled wind is directed upward and must consequently be balanced by strong eddy diffusion in order to maintain the peak at the observed altitude. This effect is illustrated in Figures 9 and 10 for the two orbits. As can be seen in Figures 7 and 8, the profiles modeled with a vertical wind are narrower than those obtained with a global K coefficient. The scale heights change by a factor of 5 between the two models with and without advective winds. For orbit 734, the profile with no wind is closer to the observation, while the profile with a vertical wind fits the limb profile from orbit 1563 better.

[18] We then examine the values for K and for the total downward flux of orbit 716 and 1577. Orbit 716 corresponds to the profile of maximum brightness whereas orbit 1577 shows the lowest peak altitude with a brightness close to the average value of Table 1. We then attempt to model these extreme limb profiles to obtain limit values of these quantities. The results are summarized in Table 4 and the corresponding profiles are shown in Figures 11 and 12. The two modeled profiles successfully match the observed peak altitudes, keeping the topside scale height quite close to the observation. Data from orbit 716, provide a maximum altitude profile for the eddy diffusion parameter in the nightside Martian atmosphere and a maximum profile for the oxygen density (and consequently for the nitrogen density). The vertical profiles are plotted in Figure 13 and densities peak at 58.7 km and 74.1 km for oxygen and nitrogen respectively for orbit 716, and at 58.0 km and 69.9 km for orbit 1577. The corresponding density values are equal to 5.4×10^{10} cm^{-3} and 1.4×10^{8} cm^{-3} for orbit 716 and 1.4×10^{10} cm^{-3} and 5.5×10^{7} cm^{-3} for orbit 1577. The differences between the peak altitudes of nitrogen and oxygen can be understood by their destruction mechanisms. Indeed, nitrogen is principally consumed in reaction 1 of Table 2 while oxygen is also destroyed in a three-body reaction (reaction 4) which brings the CO_2 density into play. Note that the K_{peak} value for orbit 716 is larger than the one for orbit 1577. This is a combination of two effects. First, for orbit 1577, the peak is at low altitude and the K value is consequently lower than it would have been at the peak altitude of orbit 716. Second, the intensity of orbit 716 is the highest of all the data set and it can only be modeled using a very large flux at the top boundary. Increasing the flux also causes an increase of

Table 4. Fit Parameters and Densities at the Peak of the Limb Profile

Orbit	Type	Spatial BIN	Part	A	K(z_{peak}) cm^2 s^{-1}	Φ_O(100 km) cm-2 s^{-1}	$n_O(z_{peak})$ cm^{-3}	$n_N(z_{peak})$ cm^{-3}
0716A01	int max	1	egress	1.7×10^{13}	1.5×10^{6}	8.7×10^{10}	5.3×10^{10}	8.1×10^{7}
1577A01	alt min	4	egress	1×10^{13}	6.4×10^{5}	1.2×10^{10}	1.4×10^{10}	4×10^{7}

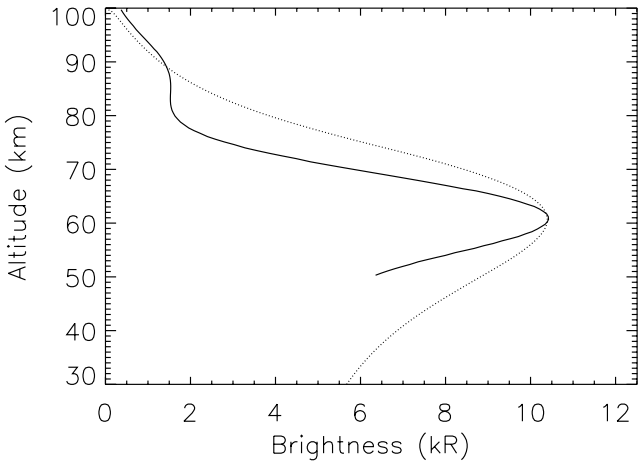

Figure 11. Observed and modeled limb profiles for orbit 716. The solid line is the observed distribution and the dotted line is the modeled profile as characterized in Table 4.

the peak altitude and thus a larger K value to maintain the peak at the correct altitude. This can be easily understood with the following formula first used by *Stewart et al.* [1980] in an attempt to explain the same behavior on Venus:

$$n(z_{peak}) = \frac{A^2}{2k|\phi_O|H^3} \tag{16}$$

where n is the atmosphere total density, k is the rate of the first reaction in Table 2 and Φ_O is the oxygen flux at the top boundary. This equation is satisfied at the peak emission altitude. Therefore if Φ_O increases, $n(z_{peak})$ will decrease, and since n(z) decreases with altitude, this change will inevitably lead to a higher value for z_{peak}.

[19] In Figure 14, we note that the profiles adopted by *Nair et al.* [1994] and *Krasnopolsky* [2006] (see Table 5) which are based on the previous speculations about eddy diffusion are larger than the profile adopted to model the observations. It is also almost exponential and monotically increases with the altitude. However, the profile used by

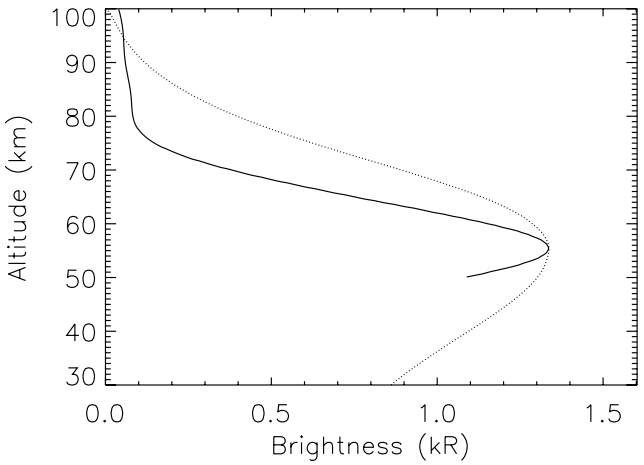

Figure 12. Observed and modeled limb profiles for orbit 1577. The solid line is the observed distribution and the dotted line is the modeled profile as characterized in Table 4.

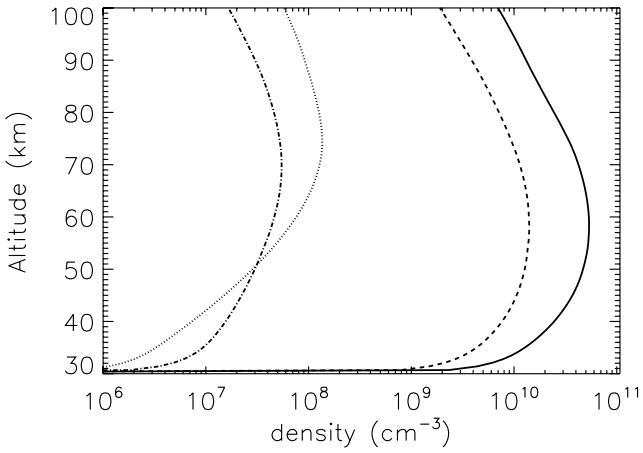

Figure 13. O and N density profiles. The solid line and the dotted line are the oxygen and the nitrogen density profiles from orbit 716 respectively. The dashed line and the dotted-dashed line are the oxygen and the nitrogen density profiles deduced from orbit 1577, respectively.

Krasnopolsky [2002] for the upper atmosphere (>80 km) stands between the K(z) values of orbits 1577 and 716.

5. Conclusions

[20] The NO nightglow emission is a good tracer of atmosphere dynamics in the Martian nightside atmosphere between 30 km and 100 km. The nightside lower thermosphere of the planet remains relatively unexplored, especially the minor constituents densities and their dynamics. SPICAM observation of the NO nightglow provide a set of limb profiles data which have been used to analyze the NO vertical distribution in details.

[21] The main observed feature is the very high variability in the NO nightglow emission, both in the altitude of the peak as well as the peak brightness. The peak altitude varies with a range of 37 km and the brightness changes by over two orders of magnitude. Locations of observation present-

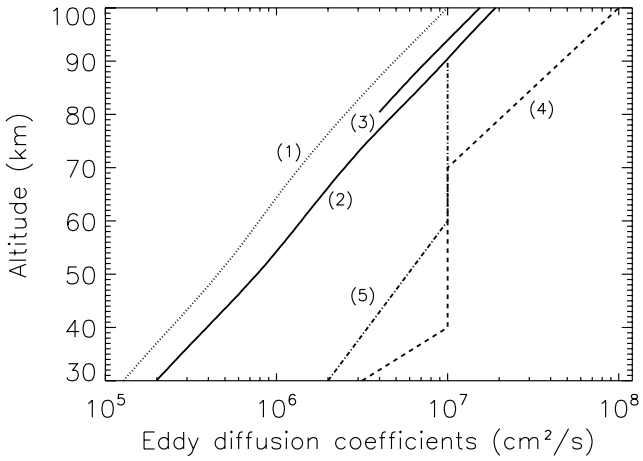

Figure 14. Eddy diffusion vertical distribution for Mars. (1) comes from the fit to the limb profile of orbit 1577. (2) is deduced from the limb profile of orbit 716. (3) is the K(z) profile adopted by *Krasnopolsky* [2002] while (4) and (5) are, respectively, the profiles used by *Nair et al.* [1994] and *Krasnopolsky* [2006] in their models of Martian phochemistry.

Table 5. Eddy Diffusion Coefficients

References	K Values, $cm^2\ s^{-1}$
Krasnopolsky [2006]	30 km: $1-3 \times 10^6$; 60 km: 10^7; 80 km: 10^7
Krasnopolsky [2002]	80–100 km: $1.7 \times 10^{13} \times n(z)^{-1/2}$
Nair et al. [1994]	0 km: 10^5; 40 km:10^7; 70 km: 10^7; 100 km: 10^8 [a]

[a]Values are typically proposed for the dayside.

ing emission below the SPICAM threshold are sometimes located close to those showing a peak on other occasions. We therefore highlight a large variability, depending on the season as well as on the latitude position or local time. Our correlative study suggests that latitude partly controls these variations, with the larger brightness values observed at low latitudes. Nevertheless, some average results obtained in this study are relevant to future comparisons with GCM simulations. We derive a mean vertical brightness, taken from Chapman fitting, of 36 R, that we have linked to a vertical flux of N equal to $7 \times 10^7\ cm^{-2}\ s^{-1}$.

[22] From the comparison with a one-dimensional chemical-diffusive model, we have determined values for the eddy diffusion coefficient and for the oxygen and nitrogen density profiles. Oxygen and nitrogen density profiles present a peak near 60 km and 70 km. Oxygen profiles are in reasonable agreement with the nighttime profiles by *Krasnopolsky* [2006, Figures 7 and 10]. We have shown that our analysis provides K values larger by about an order of magnitude than those used in earlier models, with the exception of the K(z) formulation proposed above 80 km by *Krasnopolsky* [2002]. We have also illustrated the advection effect in a one-dimensional model. The explicit presence of a vertical wind modifies the scale height of the emission profiles but does not necessarily provide a better fit to the observations. Most of the fitted profiles are similar to those illustrated in Figures 7 and 8 where observational profiles fall between the two model cases. Moreover, inclusion of advection terms in the model makes the eddy diffusion values increase to values similar to those derived by *Krasnopolsky* [2006] and *Nair et al.* [1994].

[23] Some improvements can be made in future work, such as consideration of the horizontal divergence flux terms as an input of the model. This would allow simulating a three-dimensional transport behavior by adding additional transport terms. This change would permit verification of the impact of horizontal versus vertical transport. Although the model fits the data reasonably well in most cases, the contribution of horizontal advection may modify the values of K and Φ and also globally improve the quality of the model fits.

[24] **Acknowledgments.** The authors thank the SPICAM and the MEX teams. J. C. Gérard is supported by the Belgian Fund for Scientific Research (FNRS). This work was funded by the PRODEX program of the European Space Agency (ESA) managed with the help of the Belgian Space Policy Office.

References

Angelats i Coll, M., F. Forget, M. A. López-Valverde, and F. González-Galindo (2005), The first Mars thermospheric general circulation model: The Martian atmosphere from the ground to 240 km, *Geophys. Res. Lett.*, *32*, L04201, doi:10.1029/2004GL021368.

Atreya, S. K., and Z. G. Gu (1994), Stability of the Martian atmosphere: Is heterogeneous catalysis essential?, *J. Geophys. Res.*, *99*, 13,133–13,145.

Banks, P. M., and G. Kockarts (1973), *Aeronomy*, Part B, Elsevier, New York.

Bertaux, J.-L., et al. (2005), Nightglow in the upper atmosphere of Mars and implications for atmospheric transport, *Science*, *307*, 566–569.

Campbell, I. M., and B. A. Thrush (1966), Behavior of carbon dioxide and nitrous oxide in active nitrogen, *Trans. Faraday Soc.*, *62*, 3366–3374.

Campbell, I. M., and C. N. Gray (1973), Rate constants for O(3P) recombination and association with N (4S), *Chem. Phys. Lett.*, *18*(4), 607–609.

Cohen-Sabban, J., and A. Vuillemin (1973), Ultra-violet nightglow spectrum from 1900 Å to 3400 Å, *Astrophys. Space Sci.*, *24*, 127–132.

Dalgarno, A., J. F. Babb, and Y. Sun (1992), Radiative association in planetary atmospheres, *Planet. Space Sci.*, *40*, 243–246.

Feldman, P. D., H. W. Moos, J. T. Clarke, and A. L. Lane (1979), Identification of the UV nightglow from Venus, *Nature*, *279*, 221–222.

Forget, F., F. Hourdin, R. Fournier, C. Hourdin, and O. Talagrand (1999), Improved general circulation models of the Martian atmosphere from the surface to above 80 km, *J. Geophys. Res.*, *104*, 24,155–24,175.

Fox, J. L. (1994), Rate coefficient for the reaction N+NO, *J. Geophys. Res.*, *99*, 6273–6276.

Fox, J. L. (1996), The Martian thermosphere/ionosphere at high and low solar activities, *Adv. Space Res.*, *17*, 203–218.

Gérard, J.-C., A. I. F. Stewart, and S. W. Bougher (1981), The altitude distribution of the Venus ultraviolet airglow and implications on vertical transport, *Geophys. Res. Lett.*, *8*, 633–636.

Groth, W., D. Kley, and U. Schurath (1971), Rate constant for the infrared emission of the $NO(C^2\Pi \rightarrow A^2\Sigma^+)$ transition, *J. Quant. Spectrosc. Radiat. Transfer.*, *11*, 1475–1480.

Kahn, R. (1990), Ice haze, snow, and the Mars water cycle, *J. Geophys. Res.*, *95*, 14,677–14,693.

Kong, T. Y., and M. B. McElroy (1977), The global distribution of O_3 on Mars, *Planet. Space Sci.*, *25*, 839–857.

Krasnopolsky, V. A. (1993), Photochemistry of the Martian atmosphere (mean conditions), *Icarus*, *101*, 313–332.

Krasnopolsky, V. A. (2002), Mars' upper atmosphere and ionosphere at low, medium, and high solar activities: Implications for evolution of water, *J. Geophys. Res.*, *107*(E12), 5128, doi:10.1029/2001JE001809.

Krasnopolsky, V. A. (2006), Photochemistry of the Martian atmosphere: Seasonal, latitudinal, and diurnal variations, *Icarus*, *185*, 153–170.

Krasnopolsky, V. A., and V. A. Parshev (1979), Ozone and photochemistry of the Martian lower atmosphere, *Planet Space Sci.*, *27*, 113–120.

Leblanc, F., J. Y. Chaufray, J. Lilensten, O. Witasse, and J.-L. Bertaux (2006), Martian dayglow as seen by the SPICAM UV spectrograph on Mars Express, *J. Geophys. Res.*, *111*, E09S11, doi:10.1029/2005JE002664.

Liu, S. C., and T. M. Donahue (1976), The regulation of hydrogen and oxygen escape from Mars, *Icarus*, *28*, 231–246.

McElroy, M. B., and T. M. Donahue (1972), Stability of the Martian atmosphere, *Science*, *177*, 986–988.

Nair, H., M. Allen, A. D. Anbar, Y. L. Yung, and R. T. Clancy (1994), A photochemical model of the Martian atmosphere, *Icarus*, *111*, 124–150.

Newman, S. M., I. C. Lane, A. J. Orr-Ewing, D. A. Newnham, and J. Ballard (1999), Integrated absorption intensity and Einstein coefficients for the O_2 $a^1\Delta_g$-$X^3\Sigma_g^-$ (0, 0) transition: A comparison of cavity ringdown and high resolution Fourier transform spectroscopy with a long-path absorption cell, *J. Chem. Phys.*, *110*, 10,749–10,757.

Purucker, M., D. Ravat, H. Frey, C. Voorhies, T. Sabaka, and M. Acuña (2000), An altitude-normalized magnetic map of Mars and its interpretation, *Geophys. Res. Lett.*, *27*, 2449–2452.

Shimazaki, T. (1989), Photochemical stability of CO_2 in the Martian atmosphere: Reevaluation of the eddy diffusion coefficient and the role of water vapor, *J. Geomagn. Geoelectr.*, *41*, 273–301.

Stewart, A. I., D. E. Anderson, L. W. Esposito, and C. A. Barth (1979), Ultraviolet spectroscopy of Venus: Initial results from the Pioneer orbiter, *Science*, *203*, 777–779.

Stewart, A. I. F., J.-C. Gerard, D. W. Rusch, and S. W. Bougher (1980), Morphology of the Venus ultraviolet night airglow, *J. Geophys. Res.*, *85*, 7861–7870.

Von Zahn, U., K. H. Fricke, H. J. Hoffmann, and K. Pelka (1979), Venus: Eddy coefficients in the thermosphere and in the inferred helium content of the lower atmosphere, *Geophys. Res. Lett.*, *6*, 337–340.

Yung, Y. L., and W. B. Demore (1982), Photochemistry of the stratosphere of Venus: Implications for atmospheric evolution, *Icarus*, *51*, 199–247.

Yung, Y. L., J. S. Wen, J. P. Pinto, M. Allen, K. K. Pierce, and S. Paulson (1988), HDO in the Martian atmosphere: Implications for the abundance of crustal water, *Icarus*, *76*, 146–159.

J.-L. Bertaux and A. Reberac, Service d'Aéronomie, Université Versailles Saint Quentin, CNRS, Verrières-le-Buisson, France.

C. Cox, J.-C. Gérard, and A. Saglam, LPAP, Université de Liège, Liège B-4000, Belgium. (cedric.cox@ulg.ac.be)

F. González-Galindo, Laboratoire de Météorologie Dynamique, CNRS, Paris, France.

F. Leblanc, Osservatorio Astronomico di Trieste, INAF, Trieste, Italy.